

Cite this: *RSC Adv.*, 2015, 5, 103000

# Preparation of anti-corrosion superhydrophobic coatings by an Fe-based micro/nano composite electro-brush plating and blackening process

Yan Wei, Liu Hongtao\* and Zhu Wei

Superhydrophobic coatings with high strength and corrosion resistance on hard metal surfaces have been attracting significant attention in recent years. In this paper, a quick and easy method using Fe-based micro/nano composite electro-brush plating and subsequent modification with stearic acid was established for fabricating superhydrophobic surfaces on A3 steel plates. The processing parameters including the working voltage, the brushing speed and the micro-TiO<sub>2</sub> particle concentration were studied to determine their influences on the wettability. A blackening process was conducted to further improve the corrosion resistance of the Fe-based plating layer with high water repellency. The surface morphology and chemical composition were analyzed by scanning electron microscopy (SEM) and energy dispersive spectroscopy (EDS). Corrosion resistance ability was measured using an electrochemical workstation. The results suggested that: the rough structure of the superhydrophobic coatings can be successfully fabricated by electro-brush plating technology with appropriate parameters; after post-treatment by stearic acid, the contact angle of the composite coating was up to 156° and the sliding angle was even as low as 1° under the optimal process. Meanwhile blackening treated superhydrophobic coatings still maintained excellent superhydrophobicity and the self-corrosion potential improved by 0.116 V compared to the untreated brush plating layer and the prepared superhydrophobic coatings achieved an excellent long term anti-corrosion performance.

Received 12th August 2015  
Accepted 18th November 2015

DOI: 10.1039/c5ra15640h

www.rsc.org/advances

## 1. Introduction

In the field of surface science and engineering, superhydrophobic surfaces<sup>1</sup> have received significant attention and extensive study because of their excellent properties, including self-cleaning,<sup>2</sup> oil-water separation,<sup>3</sup> anti-corrosion,<sup>4</sup> drag-reduction,<sup>5</sup> anti-icing,<sup>6</sup> *etc.* Superhydrophobic surfaces are widely existent in nature, for example lotus and watermelon leaves,<sup>7,8</sup> water strider legs,<sup>9</sup> and butterfly wings. Many researchers have investigated the characteristics of lotus leaves and found their superhydrophobicity to be determined by the interaction of micro/nano-structures and a low surface energy waxy material.<sup>8,10–13</sup> This discovery provided a model for the preparation of biomimetic superhydrophobic surfaces on many substrates. The surface wettabilities are classified into two major states: the Wenzel<sup>13,14</sup> and Cassie–Baxter<sup>15</sup> models. For rough surfaces, they play an important guiding role in studying the wetting mechanism that provides the theoretical basis for designing and preparing superhydrophobic surfaces. The micro structures and low surface energy material are the main considerations in manufacturing superhydrophobic surfaces. Therefore there are two ways to make surfaces

superhydrophobic: one is to fabricate micro/nano roughness directly onto a low surface energy material substrate such as polytetrafluoroethylene, fluorides, *etc.*<sup>16–18</sup> and the other is to modify a rough surface by materials with a low surface energy.<sup>19,20</sup>

Carbon steel is the most important and extensively used structure material due to its outstanding properties such as high strength and toughness, easy processing and low-cost. However the poor corrosion resistance of Fe inherently restricts its practical and potential applications greatly.<sup>21</sup> Water is the main factor causing steel rust, therefore, a superhydrophobic surface is an ideal choice to achieve non-wetting properties solving the problem of iron rusts in a humid environment. For the maintenance of steel facilities in harsh environments, it would save billions of dollars for companies as well as governments, if the technology could be applied to building, bridge and industrial equipment surfaces made from iron materials. Zhang *et al.*<sup>22</sup> fabricated a superhydrophobic PEEK/PTFE composite coating by changing the curing temperature of 45 steelcoating; its contact angle was up to 161°. M. A. Frank *et al.*<sup>23</sup> achieved a superhydrophobic surface on stainless steel by changing the morphology with a sandblasting process and then modifying the low surface energy with myristic acid. Huang *et al.*<sup>24</sup> designed a superhydrophobic TiO<sub>2</sub>-nanotube-coated 316 L stainless steel with low adhesion and high

College of Materials Science and Engineering, China University of Mining and Technology, Jiangsu, Xuzhou, 221116, P. R. China. E-mail: liuht100@126.com

corrosion resistance. Some extra methods have also been reported for fabricating superhydrophobic surfaces, including template extrusion,<sup>25</sup> emulsion,<sup>26</sup> sol–gel processing,<sup>27</sup> chemical etching,<sup>28</sup> electrospinning<sup>29</sup> *etc.* However there are some deficiencies such as low mechanical strength, high cost, and sophisticated preparation processes, therefore it is very desirable and promising to develop a facile and efficient method for preparing superhydrophobic surfaces with high strengths and low costs on hard metal substrates.

Herein we present a simple and economic micro/nano composite electro-brush plating approach to create a rough coating on a hard metal that is then blackening processed to prepare a superhydrophobic surface with high strength and corrosion resistance. The influences of the working voltage, the brushing speed and the micro-TiO<sub>2</sub> particle concentration on the coating wettability and microstructure were investigated. Furthermore, we discussed the mechanism of the electro-brush plating preparation of the superhydrophobic coating, and analyzed the surface wettability and anti-corrosion performance after the blackening treatment.

## 2. Experimental

### 2.1. Materials and surface treatment

First, the commercial A3 steel plates with a size of 5 mm × 4 mm × 1 mm were mechanically polished by 400#, 600#, 800# and 1000# SiC papers to remove the surface oxide layer. After that the specimens were cleaned ultrasonically for 5 min in anhydrous ethanol to remove surface impurities and then placed in a dry box as the substrates. The solution for the

Table 1 The brush plating formula

Working procedure	Chemical constituents	Concentration (g L <sup>-1</sup> )
Electrolytic cleaning solutions	NaOH	15
	Na <sub>3</sub> PO <sub>4</sub>	40
	NaC <sub>12</sub> H <sub>25</sub> SO <sub>4</sub>	0.1
No. 2 activation solutions	H <sub>2</sub> SO <sub>4</sub>	80
	(18.4 mol L <sup>-1</sup> )	
	(NH <sub>4</sub> ) <sub>2</sub> SO <sub>4</sub>	120
	NaC <sub>12</sub> H <sub>25</sub> SO <sub>4</sub>	0.1
No. 3 activation solutions	Na <sub>3</sub> C <sub>6</sub> H <sub>5</sub> O <sub>7</sub> ·2H <sub>2</sub> O	180
	NiCl <sub>2</sub> ·6H <sub>2</sub> O	1
	H <sub>3</sub> C <sub>6</sub> H <sub>5</sub> O <sub>7</sub>	130
	C <sub>2</sub> H <sub>8</sub> N <sub>2</sub> O <sub>4</sub>	0.1
	NiSO <sub>4</sub> ·7H <sub>2</sub> O	400
Preplating solutions	NiCl <sub>2</sub> ·6H <sub>2</sub> O	20
	CH <sub>3</sub> COOH	68
	HCl (36–38%)	20
	FeCl <sub>2</sub>	600
Micro-TiO <sub>2</sub> /nano-Cu composite plating solutions	C <sub>6</sub> H <sub>8</sub> O <sub>7</sub>	120
	NiCl <sub>2</sub>	50
	CH <sub>3</sub> COONH <sub>4</sub>	40
	C <sub>2</sub> H <sub>8</sub> N <sub>2</sub> O <sub>4</sub> ·H <sub>2</sub> O	2
	Micro-TiO <sub>2</sub>	20
	Nano-Cu	5
	NaC <sub>12</sub> H <sub>25</sub> SO <sub>4</sub>	0.1

Table 2 Blackening liquid formula

Chemical constituents	Concentration (g L <sup>-1</sup> )
CuSO <sub>4</sub> ·5H <sub>2</sub> O	3
Na <sub>2</sub> HPO <sub>4</sub> ·7H <sub>2</sub> O	2
C <sub>6</sub> H <sub>8</sub> O <sub>7</sub>	2
NaC <sub>12</sub> H <sub>25</sub> SO <sub>4</sub>	1
Octaphenyl polyoxyethylene	1
Na <sub>2</sub> S <sub>2</sub> O <sub>3</sub>	8
H <sub>2</sub> SeO <sub>3</sub>	4

electric-brush plating was prepared as in Table 1 and the solution for the blackening process was prepared as in Table 2. All chemical reagents were supplied by Shantou Xilong Chemical Company Ltd (China).

### 2.2. Fabrication of the superhydrophobic coating

The dried substrates were treated with the following process: electrical cleaning → activation → preplating → plating of TiO<sub>2</sub>/Cu composite coating. The main parameters of each step are shown in Table 3. Once each process was completed, the sample was rinsed with deionized water to prevent residues from the bath from contaminating the next process. Since the iron coating is so active in the acidic environment that it is quite easy to rust, a neutralization process was conducted with a lye solution containing 5 g L<sup>-1</sup> NaOH for 10 minutes as the brush plating was completed, the specimens were rinsed with deionized water then dried. Subsequently, after immersion in an ethanol solution containing 5 g L<sup>-1</sup> stearic acid at 60 °C for 40 min and then being transferred to an oven at 60 °C for 2 hours, the micro/nano scale rough coating achieved the superhydrophobic state.

In order to further improve the surface corrosion resistance and appearance quality, the coating was blackening treated at the normal temperature for 1–6 minutes. We got a shiny black surface however its energy was too high, needing to cover a layer of low surface energy materials to obtain the superhydrophobic state. Therefore, the blackening treated specimens were immersed in an ethanol solution with a concentration of 5 g L<sup>-1</sup> stearic acid for about 40 min at 60 °C, then dried in an oven at 60 °C for 2 hours.

### 2.3. Superhydrophobic coating characterization

The water contact angle (WCA) and sliding angle (SA) were measured using a surface tension instrument (JC2000D2A,

Table 3 The brush plating and blackening process parameters

Working procedure	Voltage (V)	Time (s)	Relative speed (m min <sup>-1</sup> )
Electro-cleaning	+8	30	6–8
NO <sub>2</sub> activation	–10	30	8–10
NO <sub>3</sub> activation	+12	60	8–10
Preplating	+12	90	7–9
Composite plating	+15	120	8–12
Blackening process	—	60–600	—

China), each sample was measured with a 8  $\mu\text{L}$  deionized water drop at five different positions. The morphology and composition of all the fabricated surfaces were observed using a scanning electronic microscope (SEM, Quanta 250, FEI, America) equipped with energy dispersive spectroscopy (EDS, Quantax 400-10, Bruker, Germany), operating at an accelerating voltage of 20 kV. A step profiler (DektakXT, Bruker, Germany) was used to evaluate the coating roughness. The corrosion resistance ability of the superhydrophobic coating was analyzed using potentiodynamic polarization curves acquired by an electrochemical workstation (C350, China) in a 3.5 wt% of NaCl solution representing the corrosive environment of seawater.

### 3. Results and discussion

#### 3.1. Influence of different working voltages on the superhydrophobic surface properties

The electro-brush plating voltage was varied with values of 6 V, 9 V, 12 V, and 15 V with a plating solution containing 20  $\text{g L}^{-1}$  micro- $\text{TiO}_2$  and 5  $\text{g L}^{-1}$  nano-Cu and the remaining parameters as listed in Table 3. It was observed that the larger the voltage, the greater the efficiency of the brush plating, and the more uniform and stable the coating tended to be. However when the brushing voltage reached 15 V, the coating generated significant heat resulting in the binding force between the coating and substrate being rapidly reduced, the process became unstable and part of the coating peeled off the substrate. With the increase of the working voltage, the coating roughness increased from 375 nm at 6 V to 1405 nm at 15 V (Fig. 1b), and the contact angle gradually increased to  $156^\circ$ , meanwhile the sliding angle decreased from  $38^\circ$  to  $1^\circ$  (Fig. 1a). When the working voltage reached 15 V, the coating achieved the optimal superhydrophobic state where the contact angle and sliding angle were  $156^\circ$  and  $1^\circ$  respectively after the modification with stearic acid. Beads of water began spinning round when water was dropped onto the surface. Fig. 2 shows the contact angles

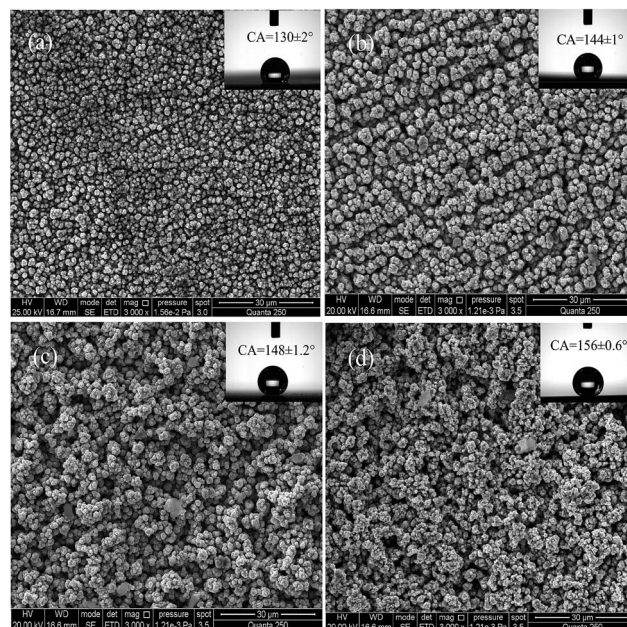


Fig. 2 The coating morphologies under different working voltages (at 3000 $\times$  magnifications). (a) 6 V, (b) 9 V, (c) 12 V, (d) 15 V.

and SEM images under different working voltages, with the working voltage increasing, the grain sizes became more and more finely distributed. The coating prepared with a working voltage of 6 V had a contact angle and sliding angle of  $130^\circ$  and  $38^\circ$ , respectively. Fig. 2a shows the corresponding coating is smooth and uniform, because the micro/nano particles and the metal ions gained electrons at a slow speed under the low plating voltage, as a consequence, the coating grew slowly and the rough structure was not obvious. Meanwhile the corresponding surface roughness was measured and the  $R_a$  value was found to be only 375 nm in Fig. 1b. With the increase of the voltage, the current density improved, however the energy

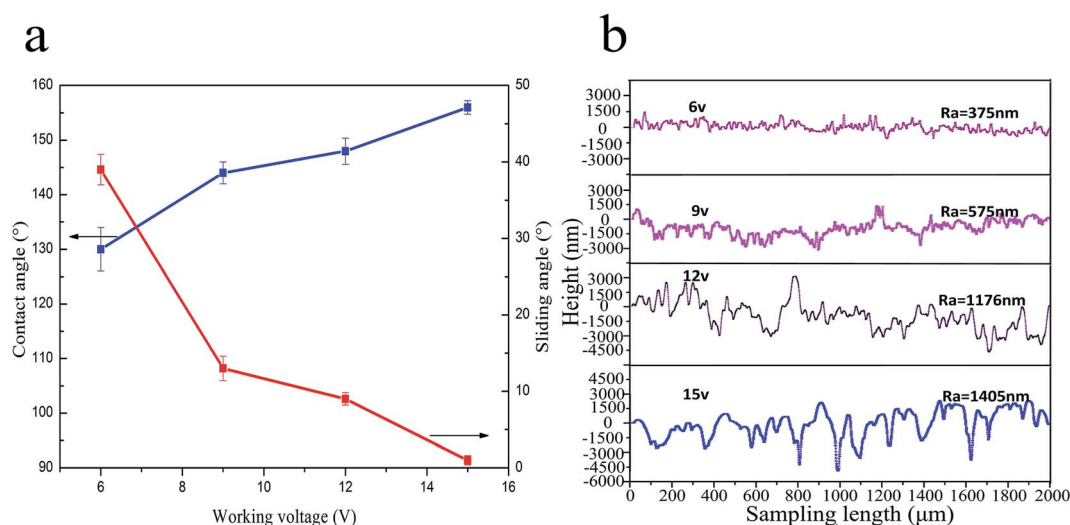


Fig. 1 (a) The contact angle and sliding angle values under different working voltages. (b) The roughness profile curves under different working voltages.



inhomogeneity stood out in the deposition process, leading to a coating surface with lots of small homogeneous protrusions<sup>30</sup> as shown in Fig. 2b. As the working voltage was increased to 12 V, the contact angle increased to 148°, and the sliding angle reduced to 9°, a remarkable change in surface morphology was observed in Fig. 2c: the coating became more uneven with more and more appearances of micro/nano dual rough structures,<sup>31,32</sup> which can be proven by the surface roughness (1176 nm). The apparent contact angle existed in the Cassie state when water droplet contacted with the rough structure surface. Fig. 2d shows an appropriate surface morphology, formed under a 15 V operating voltage, for achieving the best superhydrophobic properties; the pore structures tended to be more regular with a roughness of 1405 nm (Fig. 1b) and the grains are more finely distributed and uniform as shown in Fig. 2d. The contact angle was up to 156° and the sliding angle was only 1°, therefore water drops started rolling as soon as they touched the surface, which should be attributed to the rich porosity and rough structure.

### 3.2. The influence of brush speed on the superhydrophobic coating properties

Fig. 3 shows the relationship between the brushing speed and the coating wettability measured using 8  $\mu\text{L}$  deionized water. The brushing speed was set as 5  $\text{m min}^{-1}$ , 9  $\text{m min}^{-1}$ , 13  $\text{m min}^{-1}$ , and 17  $\text{m min}^{-1}$  while the remaining parameters and bath composition were kept constant as shown in Tables 3 and 1, respectively. When the brushing speed was 5  $\text{m min}^{-1}$ , an uneven coating formed with a number of granular mountain-like projections composed of many  $\sim 1 \mu\text{m}$  fine grains, which can be seen in Fig. 4a<sup>33,34</sup>, the corresponding roughness was 1136 nm. It possessed high superhydrophobicity with contact and sliding angles of 151° and 3° respectively. However, the current density was significantly increased due to the lower brush plating speed, which resulted in severe heat production, meanwhile bubbling, corrugation, abscission and cracking were detected on the composite coatings. Fig. 4b shows the

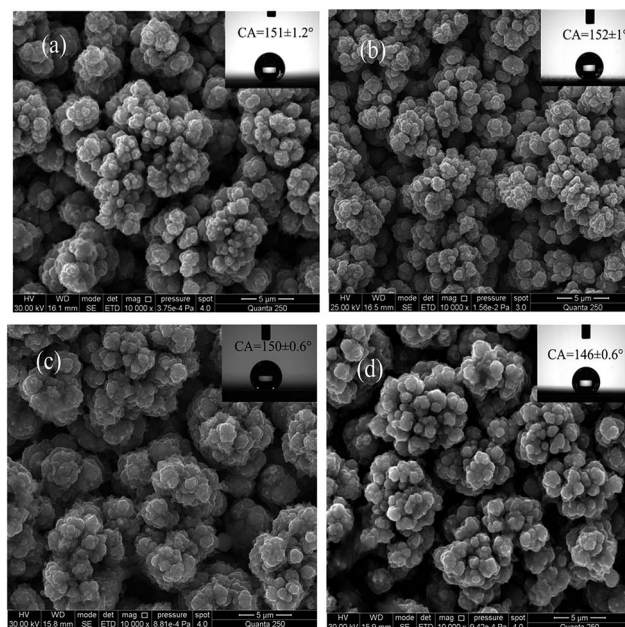


Fig. 4 The coating morphologies under different brushing speeds (at 10 000 $\times$  magnifications). (a) 5  $\text{m min}^{-1}$ , (b) 9  $\text{m min}^{-1}$ , (c) 13  $\text{m min}^{-1}$ , (d) 17  $\text{m min}^{-1}$ .

homogeneous porous structure formed from a brushing speed of 9  $\text{m min}^{-1}$ , its roughness curve (Fig. 3b) was quite regular and highly consistent with the surface morphology in Fig. 4b. It was difficult to place drops on this surface due to the higher contact angle and lower sliding angle of 152° and 2° respectively, which indicated this as an ideal brush speed as it is beneficial to the micro/nano particles mosaics, nucleation and growth. While the brushing speed was varied between 5  $\text{m min}^{-1}$  and 13  $\text{m min}^{-1}$ , the contact angle fluctuated at 150° (Fig. 3), this should be attributed to the high roughness values above 1100 nm. However it is worth noting that when the speed was up to 17  $\text{m min}^{-1}$ , the coating's grain depositions and

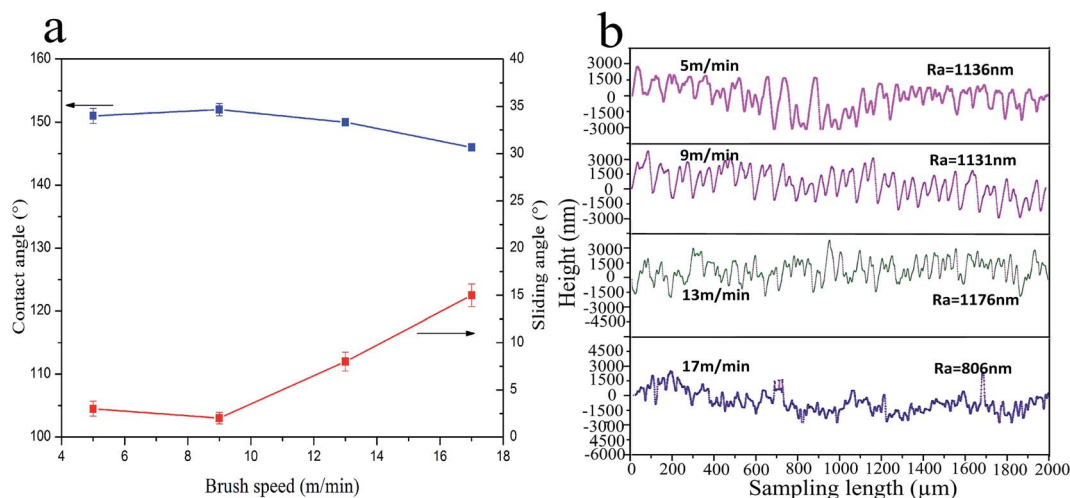


Fig. 3 (a) The contact angle and sliding angle values under different brushing speeds. (b) The roughness profile curves under different brushing speeds.

growth times were substantially reduced with metal ions nucleating on the cathode, the grains of Fe became more fine and homogeneous in agreement with the coating topography in Fig. 4d, as a consequence, the contact angle was measured and found to be only  $146^\circ$  with the sliding angle increased to  $15^\circ$ .

### 3.3. Influence of the micro-TiO<sub>2</sub> particles concentration on the performance of the superhydrophobic coating

The effect of different concentrations of micro-TiO<sub>2</sub> on the hydrophobic properties was studied by changing the micro-TiO<sub>2</sub> particles content in the plating solution. Throughout multiple experiments, the concentration of the TiO<sub>2</sub> particles was fixed at  $0\text{ g L}^{-1}$ ,  $5\text{ g L}^{-1}$ ,  $10\text{ g L}^{-1}$ ,  $20\text{ g L}^{-1}$ ,  $30\text{ g L}^{-1}$  and  $40\text{ g L}^{-1}$  while keeping the other variables constant as shown in Tables 1 and 3. A  $8\text{ }\mu\text{L}$  water droplet was used to measure the contact angle and sliding angle. It can be seen from Fig. 5a, that the contact angle firstly increases from  $139^\circ$  to  $156^\circ$  and then drastically decreases to  $138^\circ$  with the increasing of the micro-TiO<sub>2</sub> particles content, while the sliding angle decreases firstly and increases subsequently. Fig. 5b demonstrates the variation of the roughness, with the TiO<sub>2</sub> particle content increasing, the roughness increased from  $467\text{ nm}$  to  $1431\text{ nm}$  and then decreased to  $806\text{ nm}$ , which agreed with the changes of the water contact angle. According to the SEM image in Fig. 6a, it is observed that the coating with additive micro-TiO<sub>2</sub> particles of  $0\text{ g L}^{-1}$  was relatively flat with a few portions of cauliflower heads<sup>35,39</sup> consisting of bulk grains, the contact angle and surface roughness were measured and found to be only  $139^\circ$  and  $467\text{ nm}$ , respectively. Naturally it was confirmed that the coating wettability existed as the Wenzel model. When the micro-TiO<sub>2</sub> particle content was  $5\text{ g L}^{-1}$ , the contact angle reached  $145^\circ$  while the coating appeared to have more fine projections (Fig. 6b), compared with the coating preparation of  $0\text{ g L}^{-1}$ . When the micro-TiO<sub>2</sub> particles additive was  $10\text{ g L}^{-1}$ , the contact angle increased to  $150^\circ$ , the sliding angle was less than  $10^\circ$  and the roughness increased to  $1031\text{ nm}$ , therefore the Cassie state started to dominate the prepared surface, which had achieved the

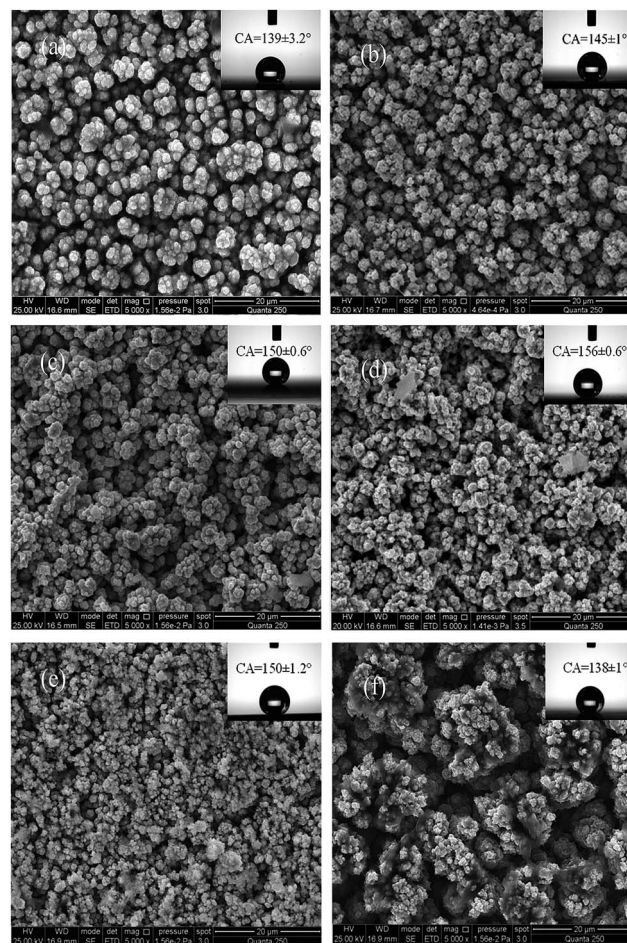


Fig. 6 The coating morphologies with different concentrations of micro-TiO<sub>2</sub> particles (at 5000 $\times$  magnifications). (a)  $0\text{ g L}^{-1}$ , (b)  $5\text{ g L}^{-1}$ , (c)  $10\text{ g L}^{-1}$ , (d)  $20\text{ g L}^{-1}$ , (e)  $30\text{ g L}^{-1}$ , (f)  $40\text{ g L}^{-1}$ .

superhydrophobic state. Some remarkable changes are presented in Fig. 6c, the porosity scale and proportion dramatically increased, at the same time even more sharp projections<sup>30</sup> can

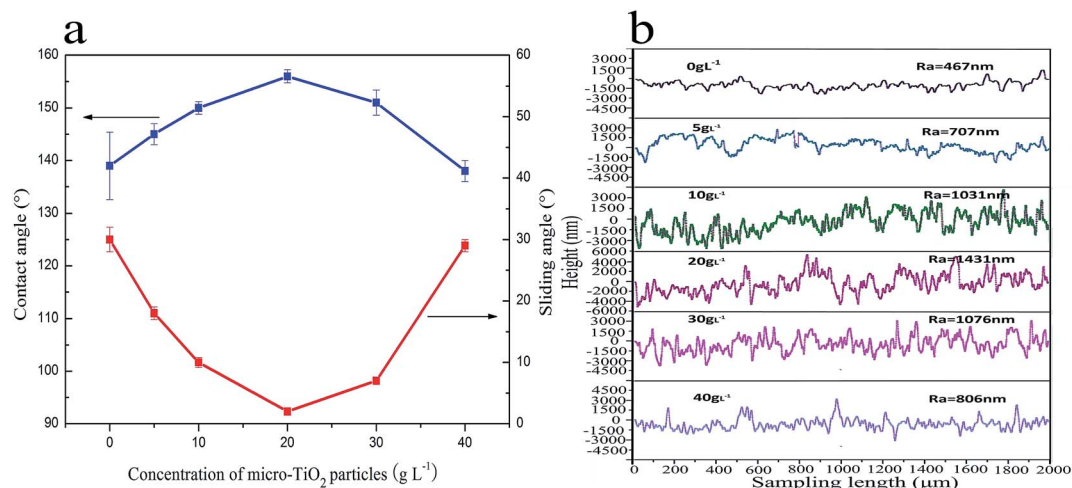


Fig. 5 (a) The contact angle and sliding angle values with different micro-TiO<sub>2</sub> particle concentrations. (b) The roughness profile curves with different micro-TiO<sub>2</sub> particle concentrations.



be observed. With the increase of the  $\text{TiO}_2$  particle content to  $20 \text{ g L}^{-1}$ , the sliding angle was  $2^\circ$  and water drops were automatically rolling without tilting the test sample, while the maximum value of the contact angle for the coatings we measured was  $156^\circ$ ; as the water drops started rolling as soon as they were placed on the coatings, the superhydrophobic coating had achieved the best performance, because of the uniform roughness curve and high  $R_a$  (1431 nm). When the micro- $\text{TiO}_2$  particle content was increased to  $30 \text{ g L}^{-1}$ , there was a slight decrease in the contact angle value at  $151^\circ$ , the corresponding rolling angle increased to  $7^\circ$  which should be attributed to the coating's poor porosity and protrusion (Fig. 6e), meanwhile the surface roughness was reduced to 1076 nm as shown in Fig. 5b. It is clearly that coatings grains becoming more fine and some regions appearing grain reunion<sup>33,34</sup> due to the sticky plating solution causing by the excess micro- $\text{TiO}_2$  particles. However, when the  $\text{TiO}_2$  particle content was  $40 \text{ g L}^{-1}$ , the SEM image Fig. 6f indicates: the morphology of the coating has undergone a tremendous change, lots of tiny grains creating larger aggregates, which is similar to a flower cluster with a diameter of

about  $10 \mu\text{m}$ , the uniform convex structure has disappeared, the coating roughness obtained only 806 nm and the spacing of some protrusions tended to be wilder in the roughness curve which is quite in keeping with the morphology in Fig. 6f. The contact angle was measured and found to be  $138^\circ$  while the sliding angle was  $29^\circ$  and water droplets are hard to roll. This is mainly due to an excess of micro- $\text{TiO}_2$  particles resulting in a sticky bath, metal ions can hardly flow freely, causing severe reunion over the particles deposition.

### 3.4. The mechanism of the electro-brush plating to prepare the superhydrophobic coating

The optimal superhydrophobic coating was investigated by EDS to analyze its surface composition. As can be seen from Fig. 7A, there are five different peaks, representing the coating which consisted of five elements Fe, Ti, O, Ni and Cu, which was consistent with the chemical composition of the plating solution. The elements of Ti and O came from the micro- $\text{TiO}_2$  particles that embedded in the coating surface during the

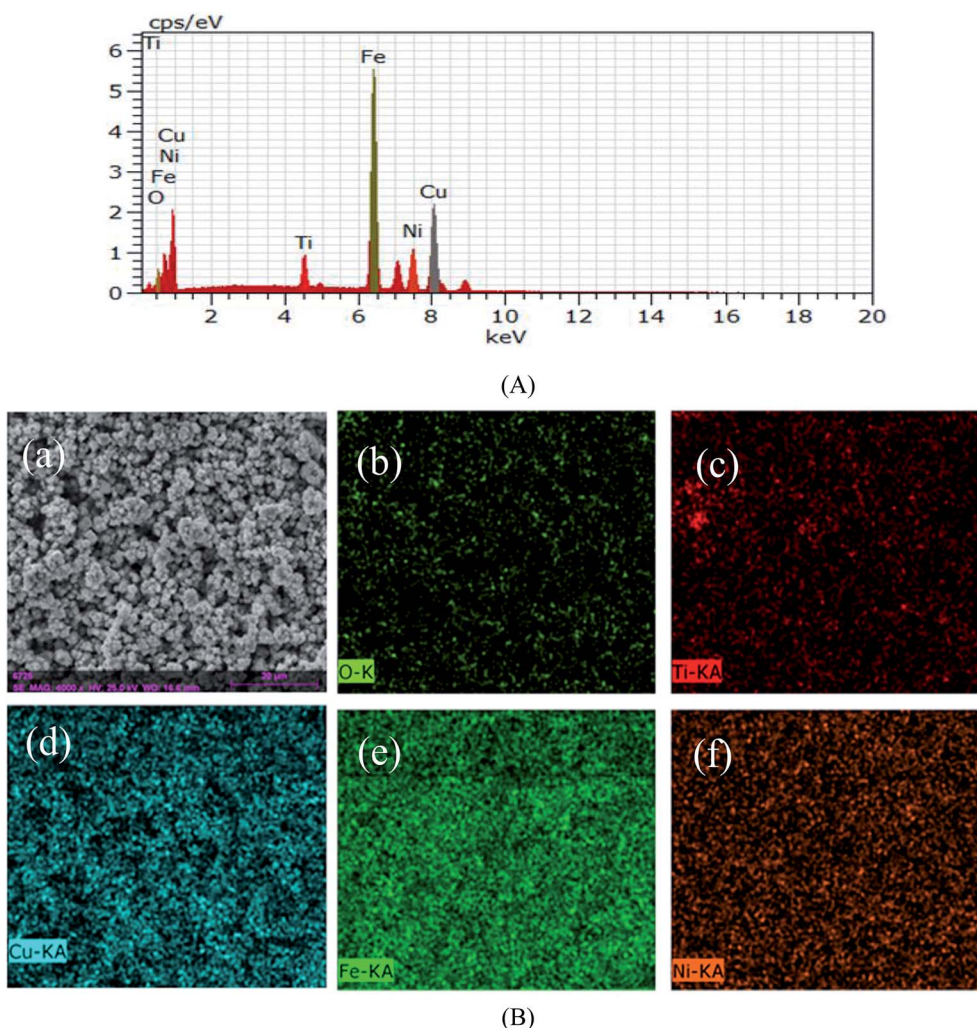


Fig. 7 (A) EDS spectrum of the optimal superhydrophobic coating (B) EDS map data of superhydrophobic coating chemical element distributions.

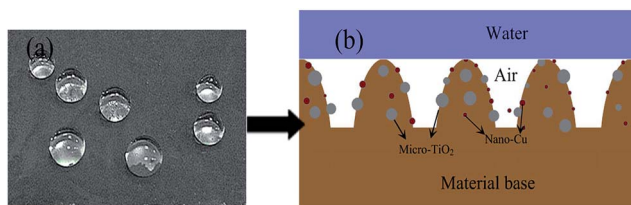


Fig. 8 (a) Optical image of water droplets on the superhydrophobic coating and (b) simplified model of the coating surface with micro structure roughness.

plating process. The Cu element on the coating surface occurs partly from the exposed nano-Cu particles of the plating layer, and partly due to the plating tip effect where a large amount of nano-Cu transformed into copper ions in the process of the nucleation and growth, which was then restored to elemental copper as a priority.<sup>35,36</sup> From the coating EDS maps of each element distribution in Fig. 7B, it is indicated that the micro/nano-particles and the metal ions of the solution have co-deposited successfully.<sup>37–40</sup> The nano-Cu particles in the electrodeposition process were mainly contributing to increasing the conductivity and current density of the bath, at the same time through synergies with the micro-TiO<sub>2</sub> during the nucleation of the composite coating they improved the nucleation rate.<sup>37</sup> Due to intermittent electrodeposition at a high current density, the cathode surface was always in an unstable state, coupled with the cutting-edge effect of the micro-nano particles, forming a rough and porous structure. This feature was very helpful for storing air to form a cushion holding water droplets, after modifying with stearic acid, the optical image of the water droplets on this structure coating is shown in Fig. 8a. The coating's convex/concave structure was observed by scanning electron microscopy and it could be simplified into a model as shown in Fig. 8b. The micro/nano roughness and porosity can catch a lot of air forming an air cushion, as a result the water can not enter into the coating holes and voids, thus obtaining the superhydrophobic state. According to water droplets in the

liquid, solid and gas three-phase composite surface proposed by Cassie, the contact angle calculation formula can be expressed as:<sup>13</sup>

$$\cos \theta_c = f_1 \cos \theta - f_2$$

where  $\theta_c$  is the apparent contact angle of the rough surface,  $\theta$  is the apparent contact angle of the smooth surface,  $f_1$  is the percentage of droplets with a solid surface occupied by the composite interface, and  $f_2$  is the percentage of water droplets in contact with the air interface ( $f_1 + f_2 = 1$ ). By measuring the A3 smooth surface and the micro/nano composite coating we can calculate the contact angle at 96° and 156°, respectively. It can be calculated that the  $f_2$  is 0.9035, obviously the air in the proportion of the compound contact interface is as high as 90.35%.

### 3.5. The morphology and composition of the blackening treated composite coating

In order to further improve the corrosion resistance and surface aesthetics for the coating while maintaining excellent superhydrophobicity, a blackening process at room temperature was an ideal choice. The morphology and composition of the blackening treated coating were determined by SEM and EDS, the results can be seen in Fig. 9. According to the SEM image (Fig. 9a), it is found that the rough structure has not been destroyed in the blackening process, with the coating still keeping its rough geometric features; this kind of convex-concave structure was inherited from the previous composite coating. As can be seen from the EDS spectra, seven different peaks are detected, demonstrating that the chemical composition of the blackening processed coatings consisted of the elements Cu, Se, P, S, Fe, C and O, which is consistent with the chemical composition of the blackening liquid. According to the relevant literature<sup>41,42</sup> and the combined analysis of the SEM image and EDS spectra, it is considered that the compositions of the black film might mainly consist of CuSe and FeSe. After being post-treated by octadecanoic acid, the contact angle of the

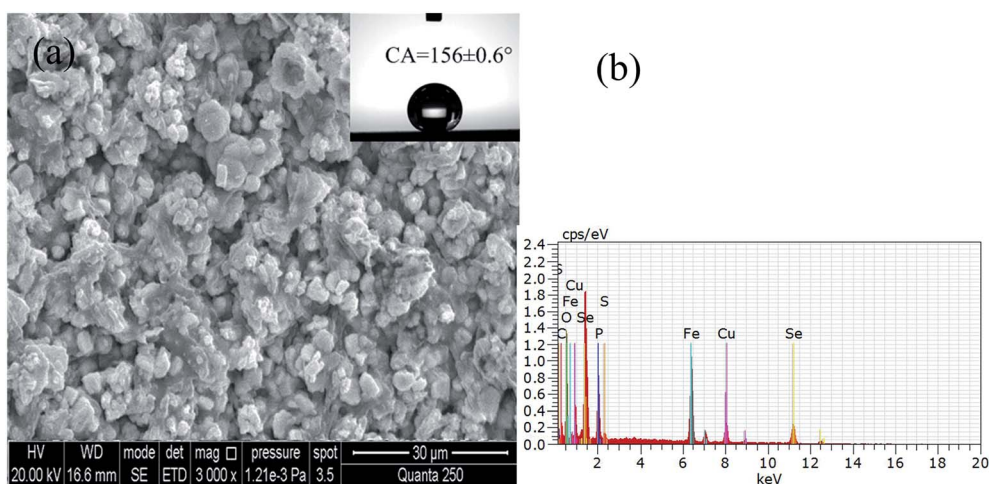


Fig. 9 The morphology and EDS data of the blackening treated coating.



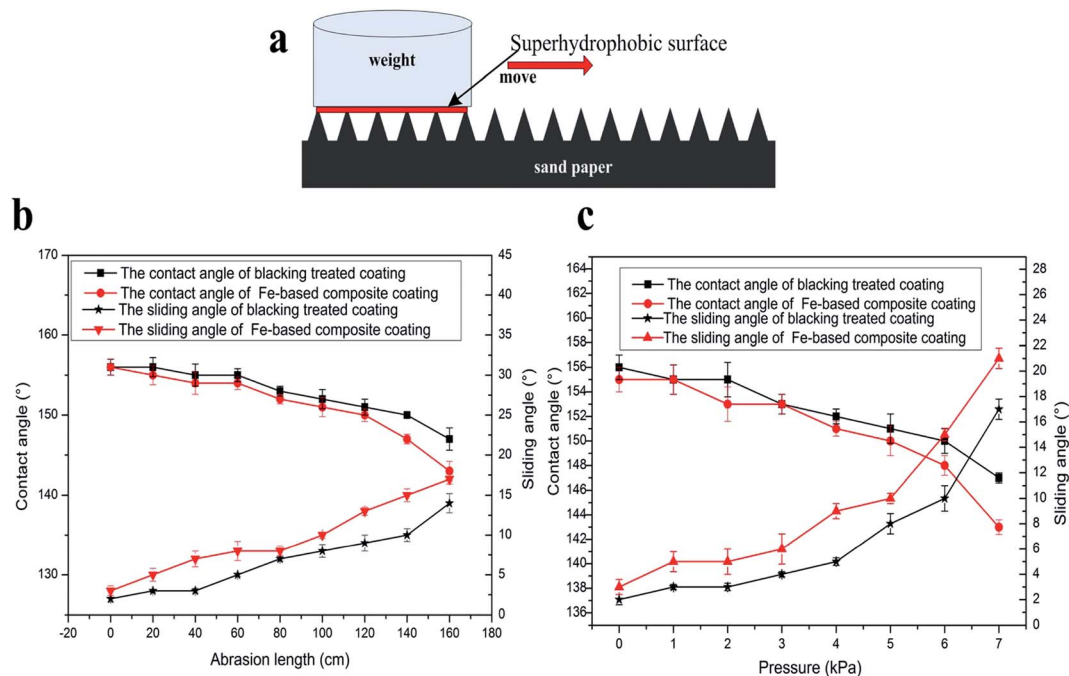


Fig. 10 (a) The schematic diagram of the scratch test, (b) the contact angle and sliding angle values of the different samples with different abrasion lengths under 4 kPa, and (c) the contact angle and sliding angle values of the different samples under different pressures after abrasion for 0.8 m.

blackening treated composite coating was up to  $156^\circ$ , the sliding angle was less than  $3^\circ$ , and it exhibited excellent water repellency.

### 3.6. Mechanical stability

The mechanical stability of the superhydrophobic surface is one of the key considerations for its practical applications. Scratch and tape-peeling tests are regarded as effective ways to evaluate the mechanical abrasion resistance. The pressure to press the tape to the sample is the “finger press” as described in the standard ASTM D 3359-09<sup>e2</sup>. The blackening treated coating can resist tape peeling 60 times by Scotch-600 adhesive tape. While the Fe-based composite coatings only survive 30 peeling times with its contact angle and sliding angle of  $150^\circ$  and  $8^\circ$ .

Therefore, the blackening treated surface achieves a better superhydrophobicity and higher binding force compared to the Fe-based composite coatings.

The schematic diagram of the scratch test is shown in Fig. 10a. We adopted 800 grit SiC sandpaper as an abrasion surface and loaded different weights on the sample. The testing contact area was  $10 \text{ mm} \times 15 \text{ mm}$ . Fig. 10b indicates that the blackening treated surface and Fe-based composite coatings still kept their superhydrophobic ability with contact angle above  $150^\circ$  and sliding angle below  $10^\circ$  after abrasion for 80 cm under 4 kPa pressure. As the sliding distance increased to 1.2 m, the Fe-based composite coatings lost their superhydrophobicity, while the blackened sample could survive 1.4 m. Fig. 10c shows the variation of the water contact angle and

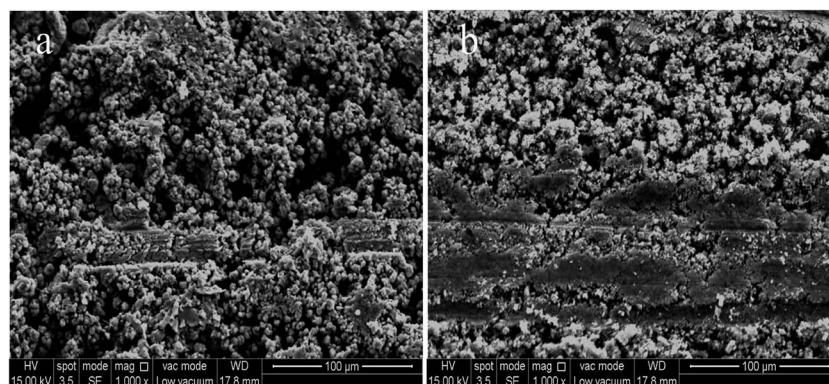


Fig. 11 The SEM morphology of (a) Fe-based composite coating and (b) blackening treated Fe-based composite coating after abrasion for 1 m at applied pressure of 5 kPa.



sliding angle under different pressures with a sliding distance of 0.8 m. With the increase of pressure, the contact angle is diminished gradually and the sliding angle becomes larger. The Fe-based composite coating firstly loses its superhydrophobicity with a pressure of 5 kPa, and with the further increasing pressure, the contact angle of the blackening treated surface decreased to  $143^\circ$  and its superhydrophobicity failed as well. While the mechanical abrasion resistance of the as prepared coatings achieved much better values than previous reports: the superhydrophobicity of a magnesium alloy is lost after 70 cm of abrasion on 800 grid sandpaper at an applied pressure of 1.2 kPa;<sup>43</sup> after 25 cm of abrasion under 3.45 kPa pressure, the superhydrophobicity of the Si surface disappeared.<sup>44</sup> The SEM images of the samples after abrasion for 1 m at 5 kPa are displayed in Fig. 11. In the Fe-based composite coatings there are some scratches covering the coating and a portion of the micro structures are damaged in the abrasion test (Fig. 11a). The blackening treated surface seems to be damaged more severely than the Fe-based composite coatings, however it still exhibits an excellent superhydrophobicity, this is due to the blackening treated surface having a much more porous and microscale structure, leading to the distribution of low surface energy material in a more dense and uniform covering on the coating (Fig. 11b).

### 3.7. The comparison of corrosion resistance with the A3 steel substrate, blackening treated A3 steel substrate, Fe-based composite coatings and blackening treated Fe-based composite coatings

Potentiodynamic polarization curves were carried out using an electrochemical workstation to investigate the anti-corrosion performances. First, the A3 steel substrate, blackening treated A3 steel substrate, Fe-based composite coatings and the

blackening treated Fe-based composite coatings were soaked in 3.5% NaCl corrosion solution stabilizing for 1 hour, then the potentiodynamic polarization curves were measured using an electrochemical workstation. An SEC electrode was used as the reference electrode, a Pt electrode as the auxiliary electrode, and the working electrode was the prepared samples with  $10\text{ mm} \times 10\text{ mm}$  exposed area. The polarization curves of the different treated samples are shown in Fig. 12; according to the fitting Tafel curves and Table 4, the A3 steel corrosion potential ( $E_{\text{corr}}$ ) and corrosion current density ( $I_{\text{corr}}$ ) are  $-0.689\text{ V}$  and  $1.04 \times 10^{-4}\text{ A cm}^{-2}$ , respectively, whereas the  $E_{\text{corr}}$  and  $I_{\text{corr}}$  of the blackening treated A3 steel substrate are  $-0.551\text{ V}$  and  $1.96 \times 10^{-5}\text{ A cm}^{-2}$ . It is obvious that the blackening film can effectively improve the steel substrate's corrosion resistance. The anti-corrosion property of the Fe-based composite coating is further improved with  $E_{\text{corr}}$  and  $I_{\text{corr}}$  values of  $-0.443\text{ V}$  and  $9.19 \times 10^{-6}\text{ A cm}^{-2}$ . After the blackening process, the superhydrophobic coating achieved its best corrosion resistance, corrosion potential decreased to  $-0.33\text{ V}$ , with a corrosion current density as low as  $3.21 \times 10^{-6}\text{ A cm}^{-2}$ , its corrosion

Table 4 The corrosion potential ( $E_{\text{corr}}$ ) and the corrosion current density ( $I_{\text{corr}}$ ) of A3 steel substrate, blackening treated A3 steel substrate, Fe-based composite coating and the blackening treated Fe-based composite coating in 3.5% NaCl solution

Sample	$E_{\text{corr}}$ (V)	$I_{\text{corr}}$ ( $\text{A cm}^{-2}$ )
A3 steel substrate	$-0.689$	$1.04 \times 10^{-4}$
Blackening treated A3 steel substrate	$-0.551$	$1.96 \times 10^{-5}$
Fe-based composite coating	$-0.443$	$9.19 \times 10^{-6}$
Blackening treated Fe-based composite coating	$-0.327$	$3.21 \times 10^{-6}$

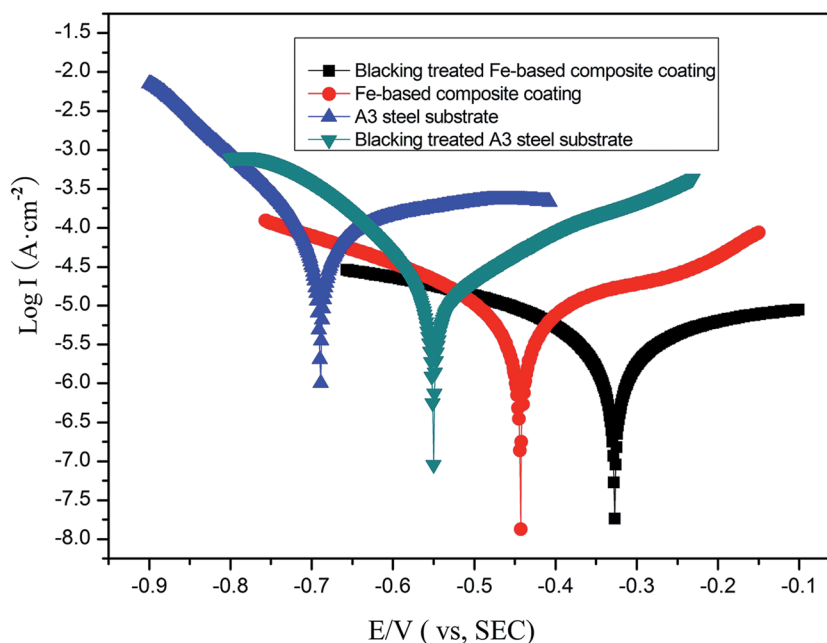


Fig. 12 Potentiodynamic polarization curves of the different process treated coatings.

potential is more positive and its corrosion current density much lower than the A3 steel substrate. Because the superhydrophobic surface coating has a lotus-like micro structure, water droplets can be separated to the surface, so the contact area between the water droplets and the superhydrophobic surface is tiny, the superhydrophobic surface could therefore effectively reduce the extent of the corrosion. It is worth noting that the blackening treated composite coating is significantly positive compared to both the superhydrophobic coating and the A3 steel substrate as shown in Fig. 12, while the corrosion resistance of the blackening treated A3 steel substrate without superhydrophobicity just has a slight improvement. Fig. 13a and b show the morphologies of the blackening treated samples, it is clear that there are only some minor micro structures on the A3 steel substrate and they are lacking the structures of convex and holes compared to the blackening treated Fe-based composite coating, which can be proved by the two samples surface roughnesses shown in Fig. 13c. Therefore, the wettability of the blackening treated A3 steel substrate was composed of Wenzel and Cassie composite states, leading to NaCl solution immersion of the coating with a poor anti-corrosion property. The deposited film of stable CuSe played an important role in improving the electrochemical stability in the corrosive environment, making self-corrosion potential move to the positive direction.

The long term corrosion test in 3.5% NaCl solution was conducted and the results are shown in Fig. 14(A). It is clear that the blackening treated coating and the Fe-based composite coating achieve a better long term anti-corrosion performance compared to the A3 steel substrate. With the increase of immersion time, the open circuit potential of the coated

samples is decreased at first, then tend to stabilise at  $-0.6$  V and  $-0.55$  V, respectively. This should be attributed to the wettability change from the superhydrophobic to hydrophilic state. However the A3 steel substrate's potential is more negative due to the lack of protection from the composite coating and blackening film.

The optical images of the A3 steel substrate, Fe-based composite coating and the blackening treated surface substrates after staying in 3.5% NaCl solution for several days can be seen in Fig. 14(B). It is clear that the A3 steel substrate has a poor anti-corrosion performance with the increasing of immersion time compared to the two superhydrophobic samples. Fig. 14(B)-a shows the corrosion firstly appeared on the A3 steel surface and the solution changes from clear to a rust-color after staying in 3.5% NaCl for 2 days, whereas the superhydrophobic substrates still keep their original state and the solution immersing the Fe-based composite coating and the blackening treated surface still remain clear and transparent. As the immersion time increases to 7 days, a small area of corrosion appeared in the Fe-based composite coating, however on the blackening treated surface only a small amount of rust could be found until immersing for 14 days in the 3.5% NaCl solution (Fig. 14(B)). Therefore, the superhydrophobic blackening treated coating could provide a long-term protection for A3 steel. Meanwhile the corresponding EIS can be seen in Fig. 14(B)(d-f). Fig. 14(B)-d shows the corrosion first appears on the A3 steel surface and the solution change shows the impedance values of the A3 steel substrate, Fe-based composite coating and the blackening treated surface substrates after immersion for 0 days; due to the existence of an air film between the water and substrate, the superhydrophobic surfaces own

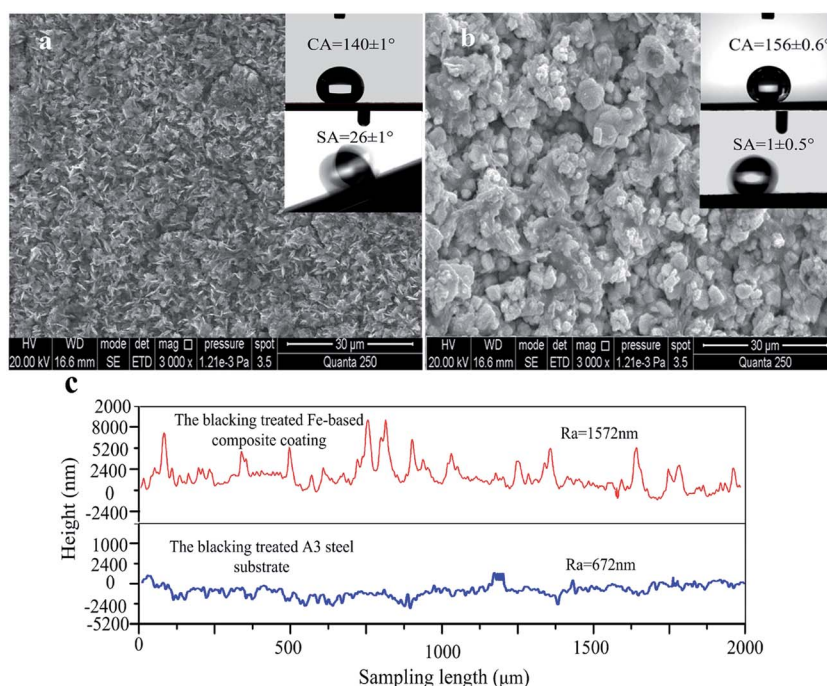


Fig. 13 The SEM morphologies of blackening treated (a) A3 steel substrate and (b) Fe-based composite coating, and (c) the surface roughness of the two samples.

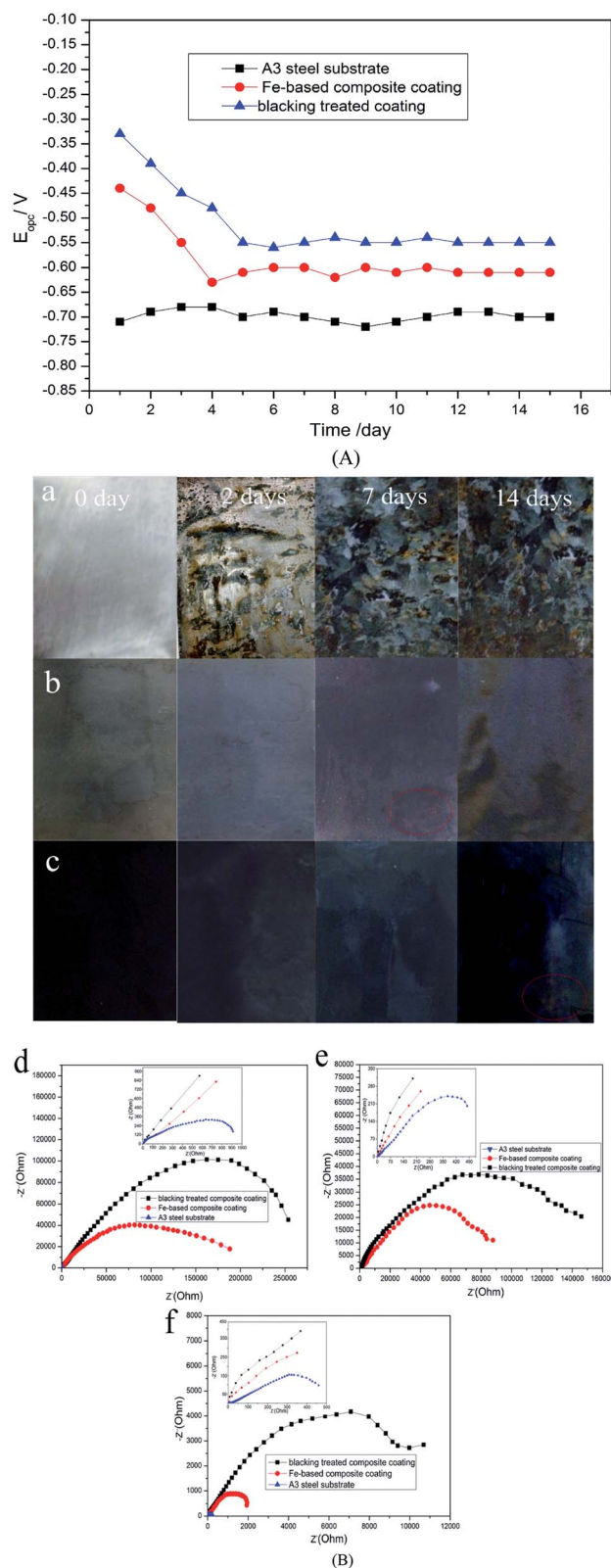


Fig. 14 (A) The open circuit potential (OCP) of the different samples versus time in 3.5% NaCl solution. (B) The optical images of the (a) A3 steel substrate, (b) Fe-based composite coatings, (c) blackening treated composite surface after staying in 3.5% NaCl solution for several days and the Nyquist plots of the different samples after immersing for (d) 0 day, (e) 2 days and (f) 14 days.

a very high impedance compared to the A3 steel substrate. After the substrates were immersed for 2 days, the impedance of the Fe-based composite coating and the blackening treated surface have suffered a great fall because their wettability has transformed into a Wenzel and Cassie composite state from the single Cassie state leading to a weakening of the air film effect. When the immersion time increases to 14 days, the impedance of the blackening treated surface is around  $10\,000\ \Omega\ \text{cm}^{-2}$ , that is much larger than the Fe-based composite coatings ( $2000\ \Omega\ \text{cm}^{-2}$ ), this is due to the blackening film having a fine and close texture.<sup>45</sup> However the A3 steel substrate's impedance minimum is only about  $400\ \Omega\ \text{cm}^{-2}$ . The excellent anti-corrosion performance of the blackening treated coating should be attributed to the combined protection effect of both the blackening film and the Fe-based composite coating (Fe-Cu-Ni).<sup>46</sup> The blackening process should not only improve its anti-corrosion ability and surface aesthetics but also add the functions of light absorption and an anti-reflective nature, which have wide prospective applications in military products.

## 4. Conclusions

In summary, a metallic superhydrophobic coating with excellent anti-corrosion performance was fabricated by micro/nano composite electro-brush plating technology and a blackening process. We analyzed the main processing factors affecting the coating's superhydrophobicity and reached some conclusions as follows: the anti-corrosion superhydrophobic coating can be successfully prepared on A3 steel by a composite brush plating and blackening process with appropriate parameters. The optimal process parameters for preparing a superhydrophobic surface are when the working voltage is 15 V, the brush plating speed is  $9\ \text{m}\ \text{min}^{-1}$ , and the concentration of the micro- $\text{TiO}_2$  particles is  $20\ \text{g}\ \text{L}^{-1}$ , nano-Cu particles is  $5\ \text{g}\ \text{L}^{-1}$ . The contact angle is up to  $156^\circ$ , and the sliding angle is as low as  $1^\circ$  after modifying with stearic acid; the contact angle of the blackening processed superhydrophobic coating still remained at  $156^\circ$ , with a sliding angle of less than  $3^\circ$ . The as prepared coatings exhibited excellent abrasion resistance and the anti-corrosion performance is greatly improved compared with superhydrophobic coating for non-blackening.

## Acknowledgements

This work was supported by the National Nature Science Foundation of China (No. 51475457) and Qing Lan Project. We express our grateful thanks to them for their financial support.

## References

- 1 A. Lafuma and D. Quere, Superhydrophobic states, *Nat. Mater.*, 2003, **2**, 457–460.
- 2 R. Blossey, Self-cleaning surfaces-virtual realities, *Nat. Mater.*, 2003, **2**, 301.
- 3 J. Zhang and S. Seeger, Polyester materials with superwetting silicone nanofilaments for oil/water separation and selective oil absorption, *Adv. Funct. Mater.*, 2011, **21**, 4699.



- 4 Y. Chen, S. Chen, F. Yu, W. Sun, H. Zhu and Y. Yin, Fabrication and anti-corrosion property of superhydrophobic hybrid film on copper surface and its formation mechanism, *Surf. Interface Anal.*, 2009, **41**, 872.
- 5 R. Truesdell, A. Mammoli, P. Vorobieff, F. Swol and C. J. Brinker, Drag reduction on a patterned superhydrophobic surface, *Phys. Rev. Lett.*, 2006, **97**, 044504.
- 6 L. Mishchenko, B. Hatton, V. Bahadur, J. A. Taylor, T. Krupenkin and J. Aizenberg, Design of ice-free nanostructured surfaces based on repulsion of impacting water droplets, *ACS Nano*, 2010, **4**, 7699–7707.
- 7 C. Extrand and W. Moon, Sung, Repellency of the Lotus Leaf: Contact Angles, Drop Retention, and Sliding Angles, *Langmuir*, 2004, **30**, 8791–8797.
- 8 A. Marmur, The lotus effect: Superhydrophobicity and metastability, *Langmuir*, 2004, **20**, 3517–3519.
- 9 X. Gao and L. Jiang, Biophysics: water-repellent legs of water striders, *Nature*, 2004, **432**, 36.
- 10 E. Bormashenko, O. Gendelman and G. Whyman, Superhydrophobicity of Lotus Leaves versus Birds Wings: Different Physical Mechanisms Leading to Similar Phenomena, *Langmuir*, 2012, **28**, 14992–14997.
- 11 L. Feng, S. Li, Y. Li, *et al.* Super-hydrophobic surfaces: from natural to artificial, *Adv. Mater.*, 2002, **14**(24), 1857–1860.
- 12 P. Roach, J. Shirtcliffe and M. Newton, Progress in superhydrophobic surface development, *Soft Matter*, 2008, **4**, 224–240.
- 13 R. N. Wenzel, Resistance of solid surfaces to wetting by water, *Ind. Eng. Chem.*, 1936, **28**, 988–994.
- 14 R. N. Wenzel, Surface roughness and contact angle, *J. Phys. Chem.*, 1949, **53**, 1466–1467.
- 15 A. Cassie and S. Baxter, Wettability of porous surfaces, *Trans. Faraday Soc.*, 1944, **40**, 546–551.
- 16 W. X. Hou and Q. H. Wang, Stable polytetrafluoroethylene superhydrophobic surface with lotus-leaf structure, *J. Colloid Interface Sci.*, 2009, **333**, 437–443.
- 17 D. W. Gong, Y. L. Jiang and P. X. Fan, Thermal stability of micro-nano structures and superhydrophobicity of polytetrafluoroethylene films formed by hot embossing via a picosecond laser ablated template, *Appl. Surf. Sci.*, 2015, **331**, 437–443.
- 18 T. Li, J. He, L. Yao and Z. Geng, Robust antifogging antireflective coatings on polymer substrates by hydrochloric acid vapor treatment, *J. Colloid Interface Sci.*, 2015, **444**, 67–73.
- 19 Z. Chen, F. Tian, A. Hu and M. Li, A facile process for preparing superhydrophobic nickel films with stearic acid, *Surf. Coat. Technol.*, 2013, **231**, 88–92.
- 20 Z. She, Q. Li, Z. Wang, C. Tan, J. Zhou and L. Li, Highly anticorrosion, self-cleaning superhydrophobic Ni-Co surface fabricated on AZ91D magnesium alloy, *Surf. Coat. Technol.*, 2014, **251**, 7–14.
- 21 B. Panda, R. Balasubramaniam and G. Dwivedi, On the corrosion behaviour of novel high carbon rail steels in simulated cyclic wet-dry salt fog conditions, *Corros. Sci.*, 2008, **50**, 1684–1692.
- 22 S. Haojie, Z. Zhaozhu and M. Xuehu, Super-hydrophobic PEEK/PTFE Composite Coating, *Appl. Phys. A: Mater. Sci. Process.*, 2008, **91**, 73–76.
- 23 M. A. Frank, A. R. Boccaccini and S. Virtanen, A facile and scalable method to produce superhydrophobic stainless steel surface, *Appl. Surf. Sci.*, 2014, **311**, 753–757.
- 24 Q. L. Huang, Y. Yang, R. Hu, *et al.*, Reduced platelet adhesion and improved corrosion resistance of superhydrophobic TiO<sub>2</sub>-nanotube-coated 316 L stainless steel, *Colloids Surf., B*, 2015, **12**, 134–141.
- 25 H. S. Hwang, S. B. Lee and I. Park, Fabrication of Rasp-berry-like superhydrophobic hollow silica particles, *Mater. Lett.*, 2010, **64**(20), 2159–2162.
- 26 T. Yang, H. Tian and Y. Chen, Preparation of superhydrophobic silica films with honeycomb-like structure by emulsion method, *J. Sol-Gel Sci. Technol.*, 2009, **49**, 243–246.
- 27 S. S. Latthe, H. Imai, V. Ganesan and A. V. Rao, Super-hydrophobic silica films by sol-gel co-precursor method, *Appl. Surf. Sci.*, 2009, **256**(1), 217–222.
- 28 K. K. Lau, J. Bico, K. B. K. Teo, M. Chhowalla, G. A. J. Amaratung, W. I. Milne, G. H. McKinley and K. K. Gleason, Superhydrophobic carbon nanotube forests, *Nano Lett.*, 2003, **3**(12), 1701–1705.
- 29 M. Ma, Y. Mao, M. Gupta, K. K. Gleason and G. C. Rutledge, Superhydrophobic fabrics produced by electrospinning and chemical vapor deposition, *Macromolecules*, 2005, **38**(23), 9742–9748.
- 30 E. Bittoun and A. Marmur, Optimizing Super-Hydrophobic Surfaces: Criteria for Comparison of Surface Topographies, *J. Adhes. Sci. Technol.*, 2009, **23**, 401–411.
- 31 X. W. Li, C. Wang and Y. Yang, Dual-Biomimetic Superhydrophobic Electrospun Polystyrene Nanofibrous Membranes for Membrane Distillation, *ACS Appl. Mater. Interfaces*, 2014, **6**, 2431–2438.
- 32 N. Gupta, S. Sasikala and D. B. Mahadik, Dual-scale rough multifunctional superhydrophobic ITO coatings prepared by air annealing of sputtered indium-tin alloy thin films, *Appl. Surf. Sci.*, 2012, **258**, 9723–9731.
- 33 B. Emami, T. M. Bucher and H. V. Tafreshi, Simulation of meniscus stability in superhydrophobic granular surfaces under hydrostatic pressures, *Colloids Surf., A*, 2011, **385**, 95–103.
- 34 M. M. Amrei and H. V. Tafreshi, Effects of hydrostatic pressure on wetted area of submerged superhydrophobic granular coatings, *Colloids Surf., A*, 2015, **465**, 87–98.
- 35 Q. Yu, Z. Zeng, W. Zhao, M. Li, X. Wu and Q. Xue, Fabrication of adhesive superhydrophobic Ni-Cu-P alloy coatings with high mechanical strength by one step electrodeposition, *Colloids Surf., A*, 2013, **427**, 1–6.
- 36 J. M. Lee, K. M. Bae, K. K. Jung, J. H. Jeong and J. S. Ko, Creation of microstructured surfaces using Cu-Ni composite electrodeposition and their application to superhydrophobic surfaces, *Appl. Surf. Sci.*, 2014, **289**, 14–20.
- 37 H. Liu, X. Wang and H. Ji, Fabrication of lotus-leaf-like superhydrophobic surfaces via Ni-based nano-composite electro-brush plating, *Appl. Surf. Sci.*, 2014, **288**, 341–348.

- 38 S. Huang, Y. Hu and W. Pan, Relationship between the structure and hydrophobic performance of Ni-TiO<sub>2</sub> nanocomposite coatings by electrodeposition, *Surf. Coat. Technol.*, 2011, **205**, 3872–3876.
- 39 Y. Qinglong, L. Wendan and L. Ping, Microstructure and Properties of Nickel-Base Nano-Y<sub>2</sub>O<sub>3</sub> Composite Coating Prepared with Electro-brush Plating, *Rare Met. Mater. Eng.*, 2012, **41**, 603–606.
- 40 L. Du, B. Xu, S. Dong, H. Yang and Y. Wu, Preparation, microstructure and tribological properties of nano-Al<sub>2</sub>O<sub>3</sub>/Ni brush plated composite coatings, *Surf. Coat. Technol.*, 2005, **192**, 311–316.
- 41 Ze. min Chen, P. Lu and J. yin Gao, Preparation and Characterization of Blackening Films in Steel Surface, *Adv. Mater. Res.*, 2012, **560**, 1084–1087.
- 42 Z. Zhongcheng, Compound-layer blackening of steel at room temperatures, *Plat. Surf. Finish.*, 2003, **90**, 49–50.
- 43 Z. She, Q. Li, Z. Wang, *et al.*, Researching the fabrication of anticorrosion superhydrophobic surface on magnesium alloy and its mechanical stability and durability, *Chem. Eng. J.*, 2013, **228**, 415–424.
- 44 Y. Xiu, Y. Liu, D. W. Hess and C. Wong, Mechanically Robust Superhydrophobicity on Hierarchically Structured Si Surfaces, *Nano technology*, 2010, **21**, 155705.
- 45 J. X. Zhang, Z. F. Wei, Y. N. Qiao, *et al.*, A New Process for Stainless Steel coloring, *Corros. Prot.*, 2004, **25**, 13–16.
- 46 Z. Ning Shi, *et al.*, Anti-oxidation and anti-corrosion properties of Ni-Fe-Cu inert metal anodes, *Chin. J. of Nonferrous Met.*, 2004, **14**(4), 591–595.